

Predictive 3D modelling of free oblique cutting with an Artificial Neural Network (ANN)-based material constitutive model and experimental validation over a wide range of conditions

F. Ducobu^{a,*}, O. Pantalé^b, B. Lauwers^c

^a*Machine Design and Production Engineering Lab, Research Institute for Science and Material Engineering, UMONS, Belgium*

^b*Laboratoire Génie de Production, INP/ENIT, Université de Toulouse, Tarbes, France*

^c*Department of Mechanical Engineering, KU Leuven & Flanders Make@KU Leuven-MaPS, Belgium*

Abstract

Modelling of the cutting process needs to move from 2D to 3D configurations to get closer to industrial applications. This study introduces a predictive 3D finite element model of free orthogonal and oblique cutting with an Artificial Neural Network (ANN)-based material flow law and experimental validation in strictly the same conditions (cutting and geometrical). The flow law based on a neural network allows simulating the cutting process based on data coming from the material characterization tests without requiring any postulate concerning the expression of the flow law. The developments are applied to the formation of continuous chips for the titanium alloy Ti6Al4V and an unseen broad range of 36 cutting conditions is considered: 2 cutting edge inclinations, 3 uncut chip thicknesses and 6 cutting speeds. The predictive performance of the model (i.e., the evaluation of the trends of fundamental variables with the absence of tuning of both numerical parameters and model features when cutting conditions are significantly modified) is high for the forces, mainly cutting and passive, and the chip thickness ratio on all 36 cutting conditions. The accuracy of the main cutting force is excellent: the average difference with the experiments is 4 %, within the experimental dispersion. No significant degradation of the results is brought

*Corresponding author. Tel.: +32 65 45 68

Email address: Francois.Ducobu@umons.ac.be (F. Ducobu)

by the apparition of the third, out-of-plane, force, which shows the ability of the model to handle orthogonal and oblique cutting configurations.

Keywords:

Oblique cutting, Finite element method (FEM), Predictive model, Artificial Neural Network (ANN)

1. Introduction

Selection of the tools and the cutting conditions in machining, but also comprehension of the influence of the process parameters on the quality of a component and its optimization, are still difficult to achieve because of the high level of complexity and the related nonlinear phenomena. In the frame of digital manufacturing and Industry 4.0, modelling the cutting process supports them, while remaining a challenging task. As highlighted by Arrazola et al. [1], most finite element (FE) models are developed in 2D (orthogonal cutting configuration usually) although industrial applications require 3D modelling.

Experimental validation of a model is a crucial step in modelling the cutting process. The experimental configuration should be as close as possible to the simulation. For the validation of orthogonal cutting, a rotational motion usually generates the cutting speed. This is often done in turning [2] or milling [3] and the diameter of the rotating workpiece must be large enough to reduce the influence of curvature on the results. Experimental configurations under strictly orthogonal cutting conditions are less often adopted, for example on broaching machines [4] or milling machines [5, 6]. If they remove the assumptions related to the rotary cutting motion, they generally allow lower cutting speeds (except on a dedicated machine, as in Afrasiabi et al. [7]). Free oblique cutting with a straight cutting edge has not yet been studied: all efforts have been concentrated on orthogonal cutting (mainly for 2D validation).

Lagrangian and Eulerian formulations are the most used for FE modelling of the cutting process. Combinations of formulations, such as Arbitrary Lagrangian-Eulerian (ALE) and Coupled Eulerian-Lagrangian (CEL), are increasingly being used to avoid (or reduce) mesh distortions [8]. The CEL formulation has recently been successfully applied to the modelling of cutting (2D orthogonal configuration): it provides accurate results with realistic chip shape and no mesh distortion. The first 3D applications are found in recent works [3, 9–12]. They cover orthogonal (free) cutting or a simple 3D operation, while free oblique cutting has yet to be studied.

The behaviour of the machined material is one of the key aspects of a FE model [1, 13]. Research is very intense in this area, leading to a growing number of constitutive material models ranging from empirical models to physical models, some including microstructure effects [13]. The empirical thermo-elasto-viscoplastic Johnson-Cook (JC) model [14] is still the most widely used to this day:

$$\sigma^y = (A + B \varepsilon^{p^n}) \left(1 + C \ln \frac{\dot{\varepsilon}^p}{\dot{\varepsilon}_0^p} \right) \left(1 - \left[\frac{T - T_{\text{room}}}{T_{\text{melt}} - T_{\text{room}}} \right]^m \right) \quad (1)$$

In this model, the flow stress, σ^y , is a function of the plastic strain, ε^p , the plastic strain rate, $\dot{\varepsilon}^p$, and the temperature, T . It is composed of 3 terms describing independently the plastic, viscous and thermal aspects. One of the points in favour of its adoption is the rather limited number of parameters to be identified, 5: A , B , C , m and n . Here, $\dot{\varepsilon}_0^p$ is the reference plastic strain rate, while T_{room} and T_{melt} are respectively the ambient (room) and melting temperature. More recent models developed on this basis, such as that of Calamaz et al. [15], increase this number of parameters (for the particular Calamaz model to 9). Other authors have also used Zerilli-Armstrong model to simulate cutting processes [16]. The best description (in theory) of the behaviour is obtained at the cost of a greater complexity of the identification process and a reduction of the link with the physical meaning of the model.

One of the problems of modelling material behaviour for cutting simulation is the identification of parameters, especially as the experimental equipment does not allow the high levels of strain, strain rate and temperature of machining to be achieved [13]. Inverse identification is an alternative, but the uniqueness of the solution is not always guaranteed [1, 13]. Early work by Özel and Altan [17] used the least squares method to identify the input parameters of a FE model in an inverse manner. Shrot and Bäker [18] then used the Levenberg-Marquardt algorithm for their identification of the material parameters. They showed that similar results (cutting forces and chip morphology) could be obtained by different sets of parameters and thus highlighted the non-uniqueness of the solution of the inverse problem. In addition to the flow stress parameters, Klocke et al. [19] also identified the damage parameters. In more recent work, such as Bosetti et al. [20] and Denkena et al. [21], the approach to the inverse identification problem is shifting from optimization to Artificial Intelligence (AI) based methods. The Downhill Simplex Algorithm (DSA) is adopted by Bergs et al. [22] and by Hardt et al. [23] for AISI 1045. Stampfer et al. [24] also chose DSA when treating AISI 4140 quenched at 3 different temperatures. In [25], Hardt et al. showed

that Particle Swarm Optimization (PSO) was more efficient in solving the inverse problem than DSA, even though the computational time is still significant. In order to reduce the computational time, an Efficient Global Optimization algorithm (EGO) was recently introduced by Kugalur Palanisamy et al. [26]. They identified simultaneously the parameters of the material constitutive model and the friction model for Ti6Al4V. Most of these works highlight the non-uniqueness of the identification and they all require the definition of the analytical expression of the constitutive model.

This paper fills the gap in the oblique cutting literature by investigating both orthogonal and free oblique 3D cutting configurations, both experimentally and numerically. An Artificial Neural Network (ANN), introduced in Pantalé et al. [27], is implemented in a FE cutting model for the first time in place of the JC analytical law. A wide range of cutting speeds (6), uncut chip thicknesses (3) and cutting edge inclination angles (2) resulting in 36 different conditions are considered to demonstrate the predictive capability of the FE model for the fundamental variables. The main objectives of a predictive model are the accurate modelling of trends in results as conditions change and the good agreement of predicted values with experimental values (exact values are not sought due to experimental dispersions). This type of model is intended to support future choices and developments without the need for experimental data. No assumptions are made about the geometry of the workpiece in the model (i.e., its width is the same as in experiments), while keeping the calculation time relevant for industrial applications. The developments are applied to the formation of continuous chips of the titanium alloy Ti6Al4V.

2. Experimental setup

A 3-axis GF Mikron VCE 600 Pro milling machine is used to perform dry orthogonal and oblique cutting tests on Ti6Al4V (grade 5 annealed at 750 °C for 1 h followed by air cooling) with the same kinematics as a shaper. As shown in Figure 1, the tungsten carbide tool (modified LCGN160602-0600-FG, CP500 from SECO) is fixed on a dedicated holder (modified CFHN-06 from SECO) and the sample to be cut is clamped in the spindle (no rotation is allowed during the test). The top of the sample has 3 ribs of 1 mm width (the width of the tool is 6 mm) and 10 mm length. The test consists of removing the top layer (its height is the uncut chip thickness, h) of a rib at the prescribed cutting speed, v_c . The cutting speed is provided by the feed rate, v_f , of the machine (maximum value of 40 m/min). The tool cutting edge inclination, λ_s , results from the relative angular

orientation of the tool and the sample. Table 1 shows the cutting conditions: 6 cutting speeds, 3 uncut chip thicknesses and 2 inclination angles, each repeated 3 times.

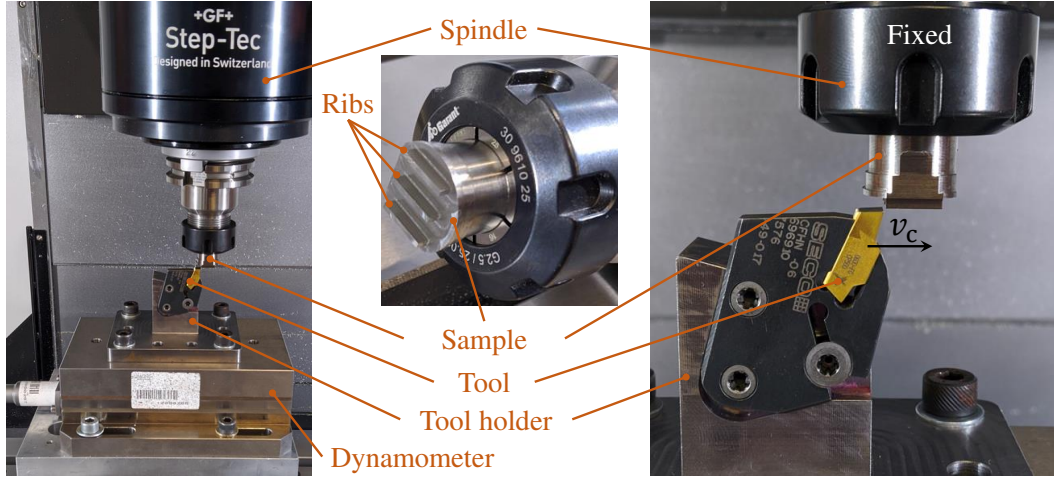


Figure 1: Experimental setup

Table 1: Cutting conditions of the study

Parameter	Values
Cutting speed, v_c (m/min)	5, 7.5, 10, 20, 30, 40
Uncut chip thickness, h (μm)	40, 60, 80
Cutting edge inclination, λ_s ($^\circ$)	0, 6
Width of the workpiece (mm)	1
Length of the workpiece (mm)	10
Width of the cutting edge (mm)	6 (1.1 in the model)
Cutting edge radius, r_β (μm)	20
Rake angle, γ_0 ($^\circ$)	15
Clearance angle, α_0 ($^\circ$)	2

Forces are measured with a 3-component Kistler 9257B dynamometer and are amplified by a Kistler 5070A charge amplifier. Acquisition is performed at 3 kHz using a Kistler 5697A2 data acquisition system and DynoWare software.

102 The recorded forces are then filtered with a second-order low-pass Bessel filter at
 103 750 Hz before calculating the average value of the steady state signal.
 104 All chips are collected and observed with a Dino Lite digital microscope
 105 AM7013MZT (5 MP, magnification 20× – 250×). Each chip is measured 3 times
 106 along its length in order to obtain an average value representative of the whole
 107 chip.

108 3. Finite element model

109 3.1. Modelling choices

110 The CEL formulation is adopted to model the dry orthogonal and free oblique
 111 cutting tests with Abaqus/Explicit 2020. The 3D model is composed of a fixed
 112 Lagrangian tool and a Eulerian part (Figure 2). Chip formation occurs by plastic
 113 flow through the Eulerian domain without mesh distortion. The Eulerian formula-
 114 tion allows for chip formation without damage properties, by removing modelling
 115 assumptions. These two features contribute to the cutting models providing accu-
 116 rate results and realistic chips [8].

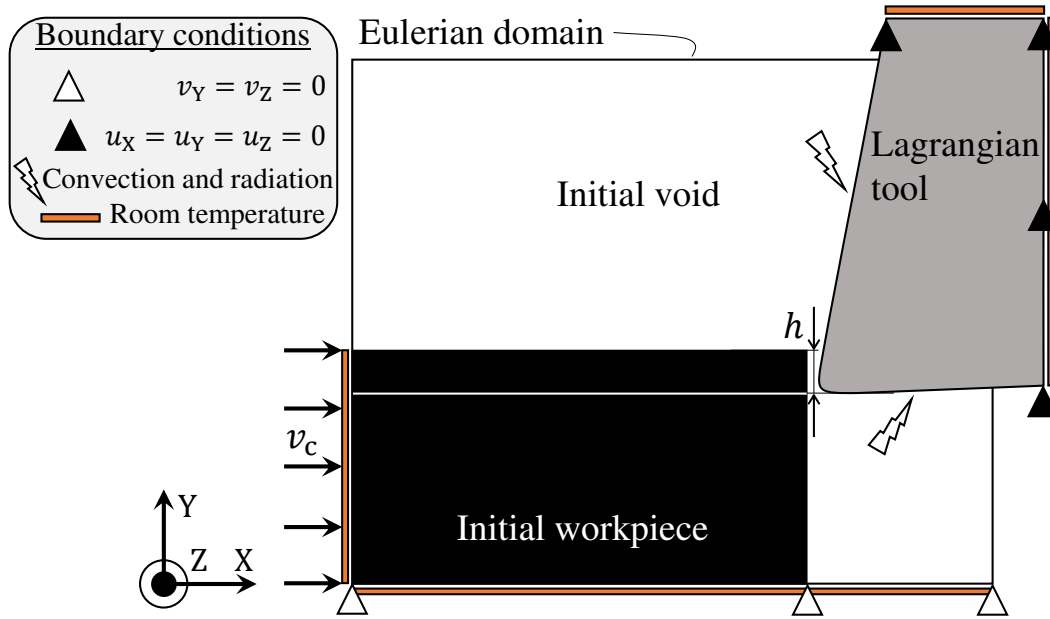


Figure 2: Boundary conditions and schematic initial geometry of the model

117 As shown in Figure 3, the full width of the workpiece (1 mm), i.e., one rib
 118 in the experiments, is modelled. To allow for chip formation and lateral flow,

119 the Eulerian domain is wider (it includes the volume in which the material can
 120 move). The volume above the initial part is also meshed with Eulerian elements
 121 for the same reasons. As in the experiments and to satisfy the assumption of
 122 an orthogonal and oblique free cut, the tool is wider than the workpiece (it is
 123 1.1 mm in the model and 6 mm in the experiments). It is very important to note
 124 that the models are the same for both inclination angles: they differ only in the
 125 rotation of the tool by 6° around the Y axis as in the experiments (Figure 3). This,
 126 together with the absence of assumptions when developing the models, contributes
 127 to make the models predictive: no input is changed when the cutting conditions
 128 are changed.

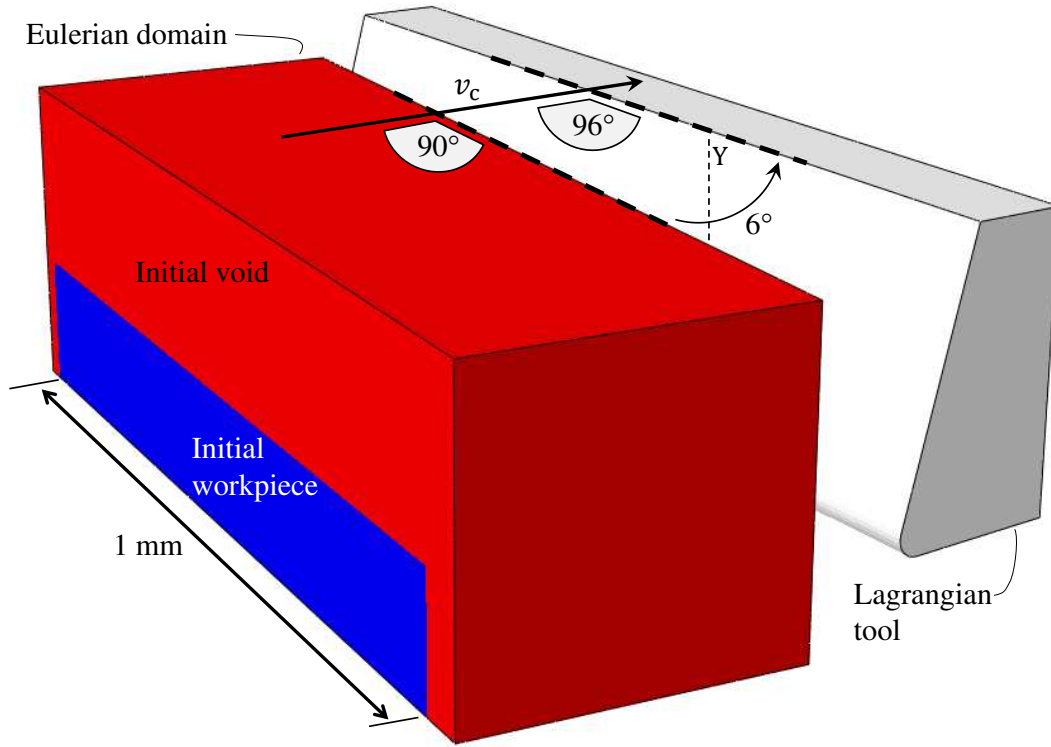


Figure 3: Configuration of the FE model for $\lambda_s = 6^\circ$

129 According to a previous sensitivity study of the mesh in orthogonal cutting
 130 with the CEL formulation [9], the edge size of the elements is $5\ \mu\text{m}$ in the plane
 131 parallel to the cutting speed. In the direction perpendicular to this plane, it is $5\ \mu\text{m}$
 132 in the areas close to the lateral boundaries of the Eulerian domain and $50\ \mu\text{m}$ in
 133 the middle of the part. To reduce the computation time, the size of the model de-

134 depends on the value of the uncut chip thickness. This results in a Eulerian domain
 135 (EC3D8RT 8-node 3D linear Eulerian elements, coupled mechanical-thermal be-
 136 haviour and reduced integration) composed of 216 550 to 273 350 nodes and a La-
 137 grangian domain (C3D8T 8-node 3D linear Lagrangian elements, coupled mechanical-
 138 thermal behaviour) of 4650 nodes.

139 The Ti6Al4V part is assumed to be thermo-elasto-viscoplastic (isotropic) and
 140 the inelastic thermal fraction is 0.9. The JC parameters set of Seo et al. [28]
 141 is adopted because the value of A corresponds to the value of the typical yield
 142 strength of Ti6Al4V and this set was found to provide the best results among the
 143 20 sets available in the literature [29]. The TiN coated tungsten carbide tool is
 144 assumed to have linear elasticity. The material properties are given in Table 2.

Table 2: Materials properties [28, 30, 31]

Young's modulus, E (GPa)	Ti6Al4V	113.8 [†]
	WC	650
Poisson's ratio, ν	Ti6Al4V	0.34
	WC	0.2
Density, ρ (kg/m ³)	Ti6Al4V	4430
	WC	14 850
Conductivity, k (W/m K)	Ti6Al4V	6.3 [†]
	WC	100
Expansion, α (1/K)	Ti6Al4V	8.6E-6 [†]
	WC	5E-6
Specific heat, c_p (J/kg K)	Ti6Al4V	531 [†]
	WC	202
JC constitutive model	A (MPa)	997.9
	B (MPa)	653.1
	C	0.0198
	m	0.7
	n	0.45
	$\dot{\epsilon}_0$ (1/s)	1
	T_{room} (K)	293
	T_{melt} (K)	1873

[†]: Dependence on the temperature, value provided at 293 K

According to the experimental results of Rech et al. [32], it is assumed that Coulomb friction occurs at the tool-piece interface and that the coefficients of

friction, μ , and heat partition, β , depend on the cutting speed. The limiting shear stress, τ_{\max} , is included and is given by:

$$\tau_{\max} = \frac{\text{yield stress}}{\sqrt{3}} = \frac{A}{\sqrt{3}} \quad (2)$$

145 All the friction energy is converted into heat. Table 3 shows the friction coeffi-
146 cients adopted in this study.

Table 3: Friction and heat transfer coefficients [30, 32]

Cutting speed, v_c (m/min)	μ	β
5	0.24	1
7.5	0.22	0.89
10	0.21	0.80
20	0.19	0.63
30	0.18	0.55
40	0.17	0.50
Limiting shear stress, τ_{\max} (MPa)	576	
Convection, U (W/m ² K)	50	
Radiation, ϵ	0.3	

147 An ambient temperature of 293 K is imposed on the top and right surfaces
148 of the tool and on the left and bottom surfaces of the workpiece (Figure 2). It
149 is assumed that radiation and convection occur on the rake and clearance faces
150 of the tool. The initial temperature of the tool and workpiece is set to the room
151 temperature (293 K). The heat transfer coefficients are provided in Table 3.

152 3.2. Material constitutive model of Ti6Al4V

153 The constitutive model of the Ti6Al4V material used in all the numerical sim-
154 ulations proposed in the section 4 is a thermo-elasto-viscoplastic law using a flow
155 criterion based on an Artificial Neural Network (ANN) identified for the cho-
156 sen material and implemented in the Abaqus/Explicit code via a Fortran subrou-
157 tine VUHARD as proposed by Pantalé et al. in [27]. The principle of this ap-
158 proach consists in replacing the analytical formulation of the flow law, based on
159 a Johnson-Cook or Zerilli-Armstrong type model, and allowing the calculation of
160 the flow stress σ^y as a function of the plastic strain ϵ^p , the plastic strain rate, $\dot{\epsilon}^p$,

161 and the temperature T , by a multi-layer ANN serving as universal approximator.
 162 Thus, the parameters of the neural network can be directly identified from the
 163 experimental data without having to postulate a behavioural model, which simpli-
 164 fies the procedure and allows greater flexibility in the definition of the model. The
 165 proposed approach also allows, as shown in Pantalé et al. [27], to compute the
 166 three derivatives of the flow stress σ^y with respect to the three input variables of
 167 the model, a necessary step to implement this model as a flow law in the form of
 168 a VUHARD subroutine in the FEM code Abaqus/Explicit, using the exact same
 169 network architecture and identified trained parameters as the one used to compute
 170 the flow stress σ^y .

171 In order to verify the influence of the neural network complexity on the nu-
 172 merical results of the simulation and on the computation time, several ANN archi-
 173 tectures are tested afterwards (in 3.4). The chosen global architecture has 2 hidden
 174 layers with a variable number of neurons for the first hidden layer ($\zeta = 9$ to 17)
 175 and 7 neurons for the second hidden layer, 3 inputs (the plastic strain, ε^p , the plas-
 176 tic strain rate, $\dot{\varepsilon}^p$, and the temperature, T) and one output (the yield strength, σ^y).
 177 The global architecture of this type of ANN is given in Figure 4 for 9 neurons in
 178 the first hidden layer. According to Pantalé et al. [27], this ANN is referred to as
 179 ANN 3-9-7-1-sig, as it has 3 inputs, 9 neurons in the first hidden layer, 7 neurons
 180 in the second hidden layer, 1 output and a sigmoid activation function.

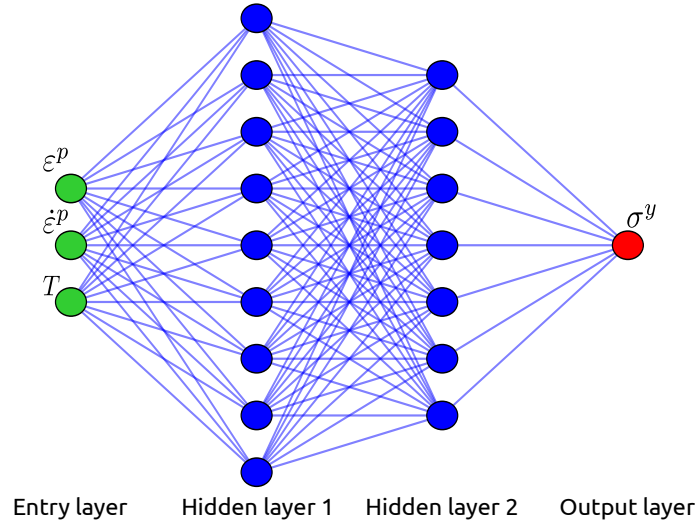


Figure 4: Architecture of the ANN 3-9-7-1-sig used for the flow law

181 In a preliminary phase, after having selected the global architecture of the neu-

ral network, it is necessary to proceed to its training from some inputs. The inputs for this application were generated from the Johnson-Cook flow law expression reported in Equation (1) and the identified parameters reported in Table 2. This approach was chosen to demonstrate the ability of the neural network flow law to replace a classically formulated flow law such as Johnson-Cook's for the simulation of metal cutting. In future developments, experimental tests on a Gleeble thermomechanical simulator will be used to generate this network training data. The training data, presented in the form of a data table containing the plastic strain ε^p , the plastic strain rate $\dot{\varepsilon}^p$, the temperature T and the flow stress σ^y , is processed by a learning algorithm, developed at LGP, in Python, using the Tensorflow library. One hour of training on a Dell XPS13 7390 laptop running Ubuntu 20.04 64 bits with 16 GiB of Ram and an Intel 4-core i7-10510U processor allow obtaining the converged parameters of the ANN model.

Once this learning phase is completed, the neural network parameters resulting from the learning process are used directly by a Python program, in charge of automatically generating the Fortran source code of the VUHARD subroutine in order to compute the flow stress σ^y and its three derivatives, required for the explicit Abaqus FEM code.

The main advantage of this approach (the use of an ANN), after the learning phase, is that, for example, the output σ^y of the network is now linked to the inputs ε^p , $\dot{\varepsilon}^p$, and T by the equations (3) to (7) for a two hidden layers neural network with a sigmoid activation function as proposed previously.

Thus, in the VUHARD subroutine, the computation of the flow stress σ^y from the 3 input variables ε^p , $\dot{\varepsilon}^p$, and T is performed using the following procedure. The first step is to scale the input data to the interval $[0, 1]$ using the following equation:

$$\vec{x} = \begin{cases} x_1 = \frac{\varepsilon^p - [\varepsilon^p]_{min}}{[\varepsilon^p]_{max} - [\varepsilon^p]_{min}} \\ x_2 = \frac{\ln(\dot{\varepsilon}^p) - [\ln(\dot{\varepsilon}^p)]_{min}}{[\ln(\dot{\varepsilon}^p)]_{max} - [\ln(\dot{\varepsilon}^p)]_{min}} \\ x_3 = \frac{T - [T]_{min}}{[T]_{max} - [T]_{min}} \end{cases} \quad (3)$$

where quantities $[]_{min}$ and $[]_{max}$ are the boundaries of the range of the corresponding field during the training phase. Corresponding values, for the proposed case, are given in Appendix A. According to the architecture of the network, the outputs of the neurons of the first hidden layer \vec{y}_1 are given by the following equation:

$$\vec{y}_1 = \text{sig}(\mathbf{w}_1 \cdot \vec{x} + \vec{b}_1) \quad (4)$$

where, \mathbf{W}_1 and \vec{b}_1 are the weights and biases associated with the first hidden layer and $\text{sig}()$ is the sigmoid activation function defined by the equation (5) :

$$\text{sig}(x) = \frac{1}{1 + e^{-x}} \quad (5)$$

Then, the output of the neurons of the second hidden layer is given by the equation (6) :

$$\vec{y}_2 = \text{sig}\left(\mathbf{W}_2 \cdot \vec{y}_1 + \vec{b}_2\right) \quad (6)$$

where, \mathbf{W}_2 and \vec{b}_2 are the weights and biases associated with the second hidden layer. Finally, the σ^y output of the ANN is thus given by the equation (7) :

$$\sigma^y = ([\sigma^y]_{\max} - [\sigma^y]_{\min}) \left(\vec{w}^T \cdot \vec{y}_2 + b \right) + [\sigma^y]_{\min} \quad (7)$$

208 where, \vec{w} and b are the weights and the bias associated with the output layer.

On the other hand, the three derivatives of the yield stress σ^y with respect to the three input variables ε^p , $\dot{\varepsilon}^p$, and T are given by the equation (8):

$$\begin{cases} \partial\sigma^y/\partial\varepsilon^p = s'_1 \frac{[\sigma^y]_{\max} - [\sigma^y]_{\min}}{[\varepsilon^p]_{\max} - [\varepsilon^p]_{\min}} \\ \partial\sigma^y/\partial\dot{\varepsilon}^p = s'_2 \frac{[\sigma^y]_{\max} - [\sigma^y]_{\min}}{[\dot{\varepsilon}^p]_{\max} - [\dot{\varepsilon}^p]_{\min}} \\ \partial\sigma^y/\partial T = s'_3 \frac{[\sigma^y]_{\max} - [\sigma^y]_{\min}}{[T]_{\max} - [T]_{\min}} \end{cases} \quad (8)$$

where s'_i is the i^{th} component of the vector \vec{s}' defined by the equation (9):

$$\vec{s}' = \mathbf{W}_1^T \cdot \left[\mathbf{W}_2^T \cdot \left(\frac{\vec{w} \circ \mathbf{e}^{-\vec{y}_2}}{[1 + e^{-\vec{y}_2}]^2} \right) \circ \left(\frac{\mathbf{e}^{-\vec{y}_1}}{[1 + e^{-\vec{y}_1}]^2} \right) \right] \quad (9)$$

209 and \circ is the elements-wise product, known as the Hadamard product. In equa-
 210 tions (3) to (9), quantities \mathbf{W}_1 , \mathbf{W}_2 , \vec{w} , \vec{b}_1 , \vec{b}_2 and b are evaluated by the training
 211 procedure of the ANN. Corresponding values for an ANN containing 9 neurons
 212 in the first hidden layer and 7 neurons in the second hidden layer are reported in
 213 Appendix A. The set of equations (3) to (9), together with the network parame-
 214 ters identified in the learning phase, is automatically translated into a VUHARD
 215 Fortran subroutine used by the FEM code Abaqus to simulate the cutting model.

216 Because of the large number of identified parameters for all the ANN models
 217 (from 114 to 202 for 9 and 17 neurons for the first hidden layer, respectively), the
 218 other 4 sets of ANN parameters used in this publication can be found in [33].

219 3.3. Sensitivity study of the results to mass scaling

220 FE modelling of the cutting process is very expensive in terms of CPU time
 221 due to the coupling of many nonlinear phenomena and the large amount of tiny
 222 finite elements. Mass scaling (MS) is introduced into the model to reduce the CPU
 223 computation time while checking that it does not influence the results (forces and
 224 energies) via a mass scaling sensitivity study. MS factors, MS_f , ranging from
 225 1E6 (theoretical CPU time scale of $\sqrt{MS_f} = 1000$) to 1 (no scale) were used for
 226 a cutting condition ($\lambda_s = 0^\circ$, $v_c = 30$ m/min and $h = 60 \mu\text{m}$). The same signal
 227 processing procedure is applied to the numerical forces as to the experimental
 228 forces (cf. 2): they are filtered with a second-order low-pass Bessel filter at 750 Hz
 229 before calculating the steady state average value. Table 4 gives the results of the
 230 model with MS normalized (\hat{F}_i) by those of the model without MS:

$$\hat{F}_i = \frac{F_i \text{ with MS}}{F_i \text{ without MS}} \quad (10)$$

231 with $i = c$ for the cutting force and $i = f$ for the feed force. As expected, the
 232 real speed-up does not increase linearly with the MS_f , but it remains significant.
 233 A MS_f of 1E6 leads to an unstable computation and a MS_f of 1E5 leads to erratic
 234 force evolutions. These results are confirmed by high values of the ratio of the
 235 kinetic (KE) to the internal (IE) energies (it should not exceed a few % [34, 35]).
 236 A value of MS_f of 1E3 is chosen as it offers a good balance between reducing the
 237 computation time and the impact on the forces, while keeping the $\frac{KE}{IE}$ below 1 %.
 238 To provide an order of magnitude of CPU computation time, between 10 h and
 239 50 h (depending on the value of h) are required on 4 cores of an Intel i7-5700HQ
 CPU at 2.7–3.5 GHz.

Table 4: MS sensitivity study (selected MS factor, MS_f , in bold, \hat{F}_c : normalized cutting force, \hat{F}_f : normalized feed force, KE : kinetic energy, IE : internal energy)

MS_f	CPU scaling	Speed-up	\hat{F}_c	\hat{F}_f	$\frac{KE}{IE}$ (%)
1	1	1	1	1	2.3E−4
1E2	10	9	1.006	0.982	2.2E−2
1E3	32	21	1.008	0.940	2.2E−1
1E4	100	61	1.012	0.921	2.4
1E5	316	173	Erratic	Erratic	22
1E6	1000	207	Unstable	Unstable	58

241 3.4. Sensitivity study of the results to the number of neurons

242 The number of neurons in the hidden layers may influence the results. A
 243 sensitivity study on the number of neurons of the first hidden layer, ζ , is performed
 244 in order to select the ANN offering the best balance between CPU computation
 245 time and quality of the results. The results of the study are provided in Table 5.
 246 \check{F}_i corresponds to the results of the model with ANN normalized by those of the
 247 model with the built-in JC model:

$$\check{F}_i = \frac{F_i \text{ with ANN}}{F_i \text{ with JC}} \quad (11)$$

248 They show no influence on the numerical results for the forces compared to the
 249 built-in Johnson-Cook model, only the computation time is influenced by the num-
 250 ber of neurons in the first hidden layer and increases with it. This increase in com-
 251 putation time is not only due to the increasing complexity of the neural network
 252 with the number of neurons, but also to the need to go through a VUHARD user
 253 subroutine. A first hidden layer of 9 neurons is therefore selected as it leads to the
 254 smallest increase in CPU computation time, without influence on the final result.

Table 5: Sensitivity of the forces to the number of neurons of the first layer, ζ (selection in bold, \check{F}_c : normalized cutting force, \check{F}_f : normalized feed force)

ζ	Time increase (%)	\check{F}_c	\check{F}_f
Built-in	0	1.000	1.000
9	6	1.000	0.999
11	6	1.001	1.000
13	7	1.000	0.998
15	8	1.001	1.001
17	10	1.000	1.000

255 4. Experimental and numerical results

256 An example of the temporal evolution of the numerical and experimental
 257 forces is plotted for the 3 directions in Figure 5 at $\lambda_s = 6^\circ$, $v_c = 10$ m/min and
 258 $h = 40$ m/min. The FE models are calculated up to a few microseconds after the
 259 stationary state is reached. Then, a linear extrapolation (dashed line between the
 260 last two markers in Figure 5) is used to provide numerical values for the same

time range as the experimental values. The average and standard deviation (2σ) are calculated from the 3 experimental values. The resulting dispersion is shown in Figure 5 around the average values of each force. Steady state takes longer to be reached for the experiments than for the numerical model, in particular for the cutting force. The dispersion around the evolution of the average force is greater for the feed force than for the cutting force, while the average value of the feed force is 46 % of the average value of the cutting force. The numerical cutting force is very close to the experimental average cutting force; it is only 4 % higher. This difference, Δj , is calculated by :

$$\Delta j = \frac{|j^{(\text{sim})} - j^{(\text{exp})}|}{j^{(\text{exp})}} \times 100 \quad (12)$$

where j is the cutting force, the feed force, the passive force or the chip thickness. $j^{(\text{sim})}$ is the average value from the simulation, while $j^{(\text{exp})}$ is the average experimental value.

The numerical feed force is underestimated by the model, but is within the 95 % experimental confidence interval. The numerical passive force difference is also underestimated and is not within the narrower experimental dispersion. The difference between the average values of the experimental and numerical feed and passive forces is 25 %. A less well modelled feed force than the cutting force is typical of FE models of the cutting process and the difference with the experimental value is similar to other studies for a narrower range of cutting conditions [7, 36–39]. Hardt and Bergs [12] also obtained larger differences for feed and passive force than for cutting force. The difference for passive force was higher than for feed force, which is the opposite observation of this work.

Numerical chips at $v_c = 10$ m/min and $h = 40$ μm for $\lambda_s = 0^\circ$ and $\lambda_s = 6^\circ$ are provided in Figures 6 and 7. When the inclination of the cutting edge is 0° , both sides of the chip are identical and a symmetry plane can be drawn in the middle of the workpiece (Figure 7 (a)). On the other hand, for an inclination of the cutting edge of 6° , the chip is no longer aligned with the workpiece. The chip bends to one side due to the orientation of the tool and symmetry is lost in both the geometry and the thermal and mechanical fields, as shown in figure 7 (b). This produces helical chips for the inclination angle of 6° as in the experiments. Figure 8 shows the variation of the chip thickness across its width: it is thicker in the middle (i.e., the body of the chip) than on its sides. This underlines the importance of 3D modelling, even for the orthogonal cutting configuration as highlighted earlier [9]. The 3D modelling also allows reproducing the lateral flow that occurs in the

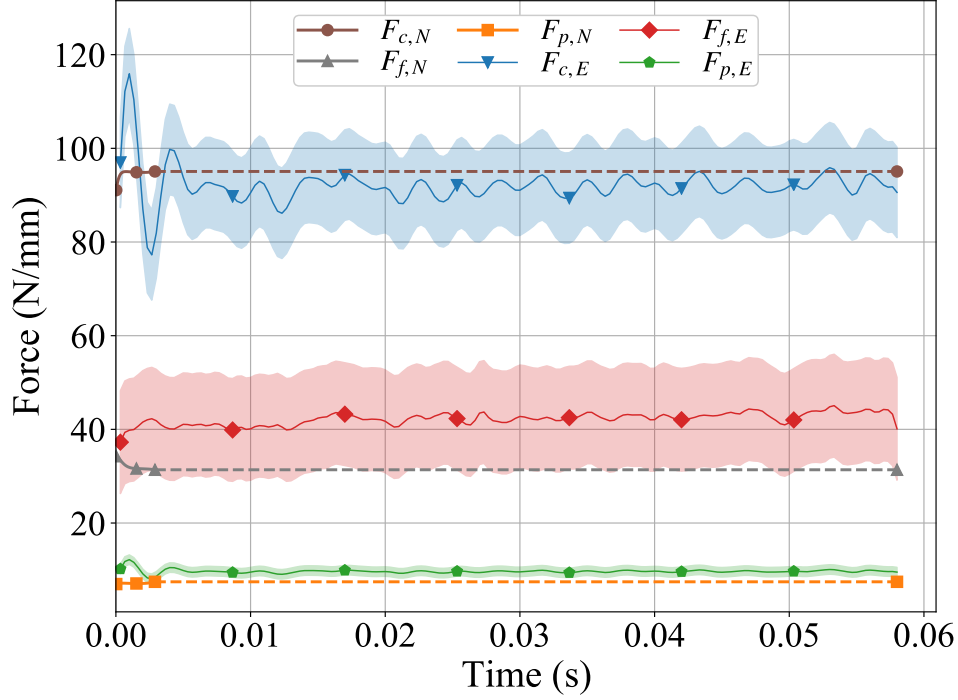


Figure 5: Temporal evolutions of experimental (E) and numerical (N) forces at $\lambda_s = 6^\circ$, $v_c = 10$ m/min and $h = 40$ μ m with dispersion around average experimental values (linear extrapolation of numerical values in dashed)

295 experiments for both values of cutting edge inclination (Figure 6), unlike a 2D
 296 model [3, 9, 10]. Although this leads to higher computation times, future cutting
 297 models should be in 3D, even when orthogonal cutting is considered. In this
 298 case, it is recommended to take advantage of the symmetry of the configuration
 299 to reduce the computation time. This simplification has not been included in this
 300 study to avoid any difference in the FE models between the 2 inclinations of the
 301 cutting edge.

302 Average values of the experimental forces and their dispersion are shown in
 303 Figures 9 to 13 together with the average numerical values. Passive force values
 304 are of course only plotted for $\lambda_s = 6^\circ$ as they are equal to zero when $\lambda_s = 0^\circ$.

305 The increase in cutting force with uncut chip thickness is clearly observed in
 306 Figures 9 and 10 for both experimental and numerical results at the 2 inclination

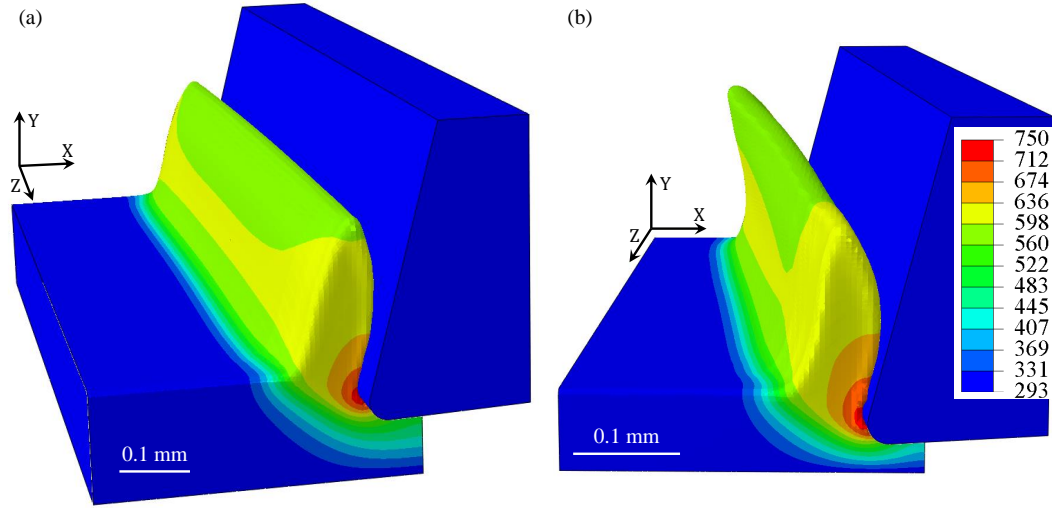


Figure 6: Temperature contours (in K) of the numerical chip after 1.5 ms at $v_c = 10$ m/min, $h = 40 \mu\text{m}$ and (a) $\lambda_s = 0^\circ$, (b) $\lambda_s = 6^\circ$

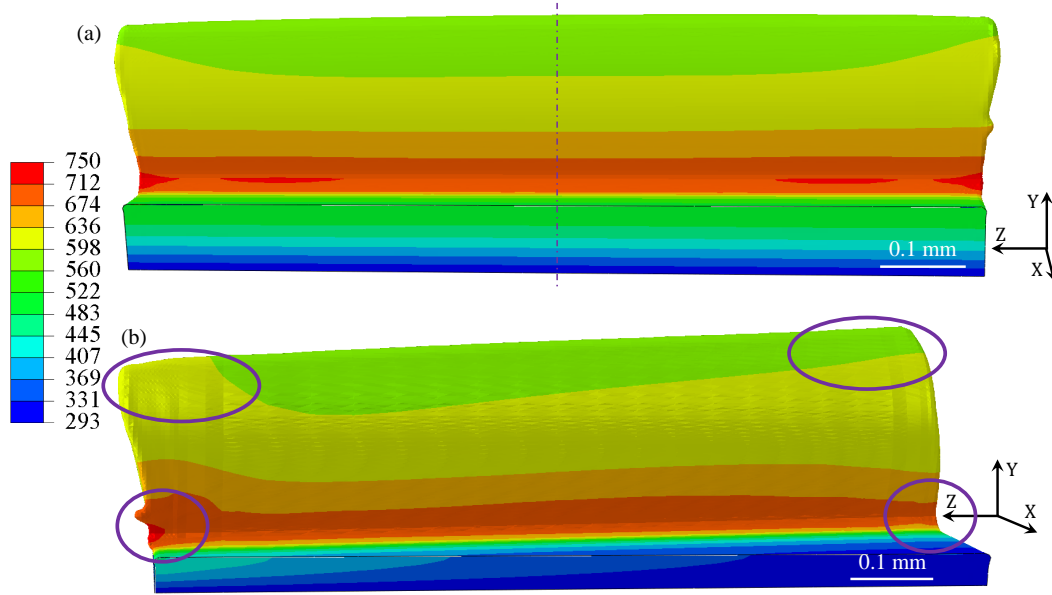


Figure 7: Temperature contours (in K) of the back of the numerical chip (tool is removed) after 1.5 ms at $v_c = 10$ m/min, $h = 40 \mu\text{m}$ and (a) $\lambda_s = 0^\circ$, (b) $\lambda_s = 6^\circ$

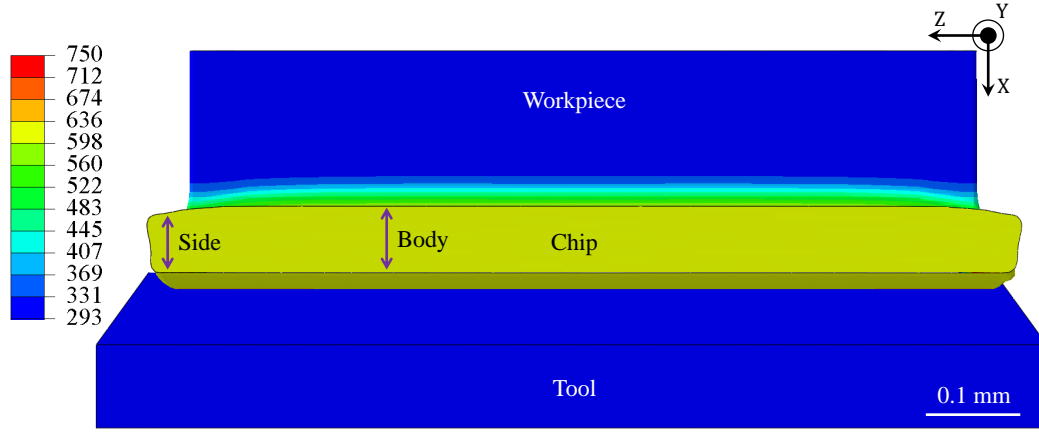


Figure 8: Temperature contours (in K) of the top of the numerical chip after 1.5 ms at $v_c = 10$ m/min, $h = 40 \mu\text{m}$ and $\lambda_s = 0^\circ$

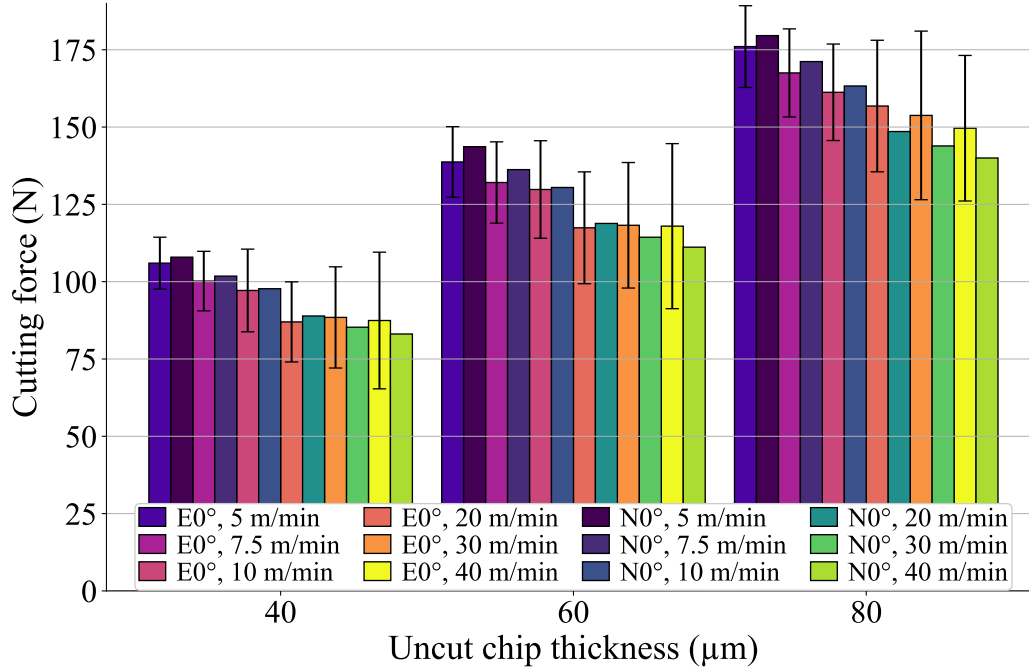


Figure 9: Comparison of experimental (E) and numerical (N) cutting forces at the cutting edge inclination of 0° for the 3 uncut chip thicknesses (40, 60 and 80 μm) and the 6 cutting speeds (5, 7.5, 10, 20, 30 and 40 m/min)

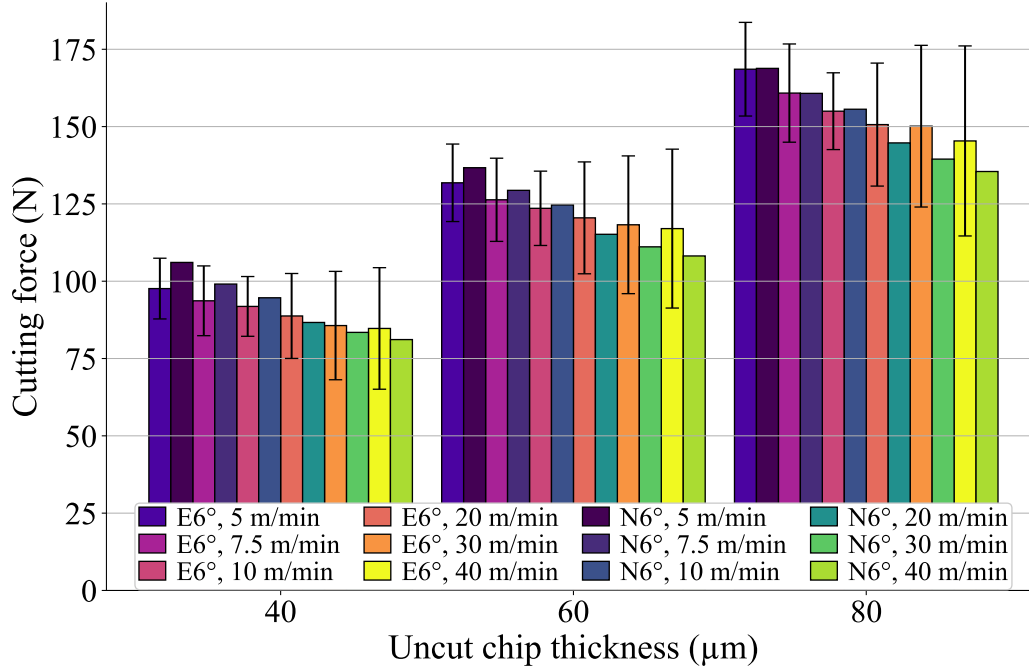


Figure 10: Comparison of experimental (E) and numerical (N) cutting forces at the cutting edge inclination of 6° for the 3 uncut chip thicknesses (40, 60 and $80\text{ }\mu\text{m}$) and the 6 cutting speeds (5, 7.5, 10, 20, 30 and 40 m/min)

307 angles, as well as the decrease in force with increasing cutting speed. This shows
 308 that temperature softening dominates strain rate hardening for Ti6Al4V and is
 309 accurately modelled. Increasing the inclination angle from 0° to 6° slightly re-
 310 duces the cutting force; this is well captured by the model. For cutting speeds of
 311 20–40 m/min and an inclination angle of 0° , F_c is almost constant with cutting
 312 speed for uncut chip thicknesses of $40\text{ }\mu\text{m}$ and $60\text{ }\mu\text{m}$, while it decreases slightly
 313 for $80\text{ }\mu\text{m}$; this small stabilization is less marked for the model.

314 An increase in the deviation around the average value with the cutting speed
 315 is noted for values above 10 m/min. All numerical values are within 95 % con-
 316 fidence of the experiments (35 of the 36 conditions are within 68 % confidence).
 317 The average difference with the experiments is 4 %, which is remarkable, also
 318 considering the wide range of cutting conditions considered and the absence of
 319 model tuning. This underlines the predictive ability and accuracy of the FE model
 320 for both inclination angles.

321 Figures 11 and 12 show the results for the feed force, where the two clearest

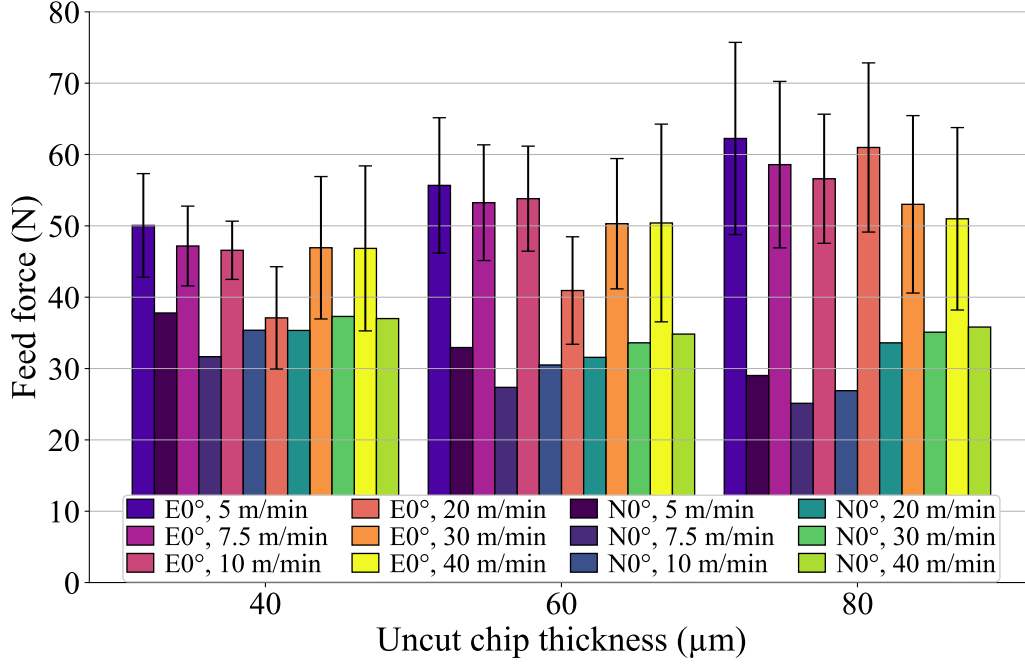


Figure 11: Comparison of experimental (E) and numerical (N) feed forces at the cutting edge inclination of 0° for the 3 uncut chip thicknesses (40, 60 and $80\text{ }\mu\text{m}$) and the 6 cutting speeds (5, 7.5, 10, 20, 30 and 40 m/min)

trends for the experiments are its decrease with the inclination angle and its in-
 crease with the uncut chip thickness (even though it is lower than expected). For
 $80\text{ }\mu\text{m}$, F_f decreases overall with v_c in the experiments. For $40\text{ }\mu\text{m}$ and $60\text{ }\mu\text{m}$, the
 force decreases at lower v_c , then increases for 0° , while a decrease is observed at
 all v_c for 6° (the experimental dispersion is high for both inclination angles, but the
 average trend with cutting speed is clear at 6° , not at 0°). For the numerical values,
 the overall trend is the same for the 3 uncut chip thicknesses and the two inclina-
 tion angles: a decrease for the lowest values of v_c and then an increase. It should
 be noted that the numerical model does not correctly handle the trends of the feed
 forces: as Figure 12 clearly shows, the numerical forces have an overall increas-
 ing trend with the cutting speed, while their average value mainly decreases when
 the uncut chip thickness increases. The differences between the average numeri-
 cal and experimental values increase with the uncut chip thickness: the forces are
 closer at $40\text{ }\mu\text{m}$ than at $80\text{ }\mu\text{m}$. The numerical values are generally not within the
 95 % confidence interval (they do not clearly change with the cutting conditions).

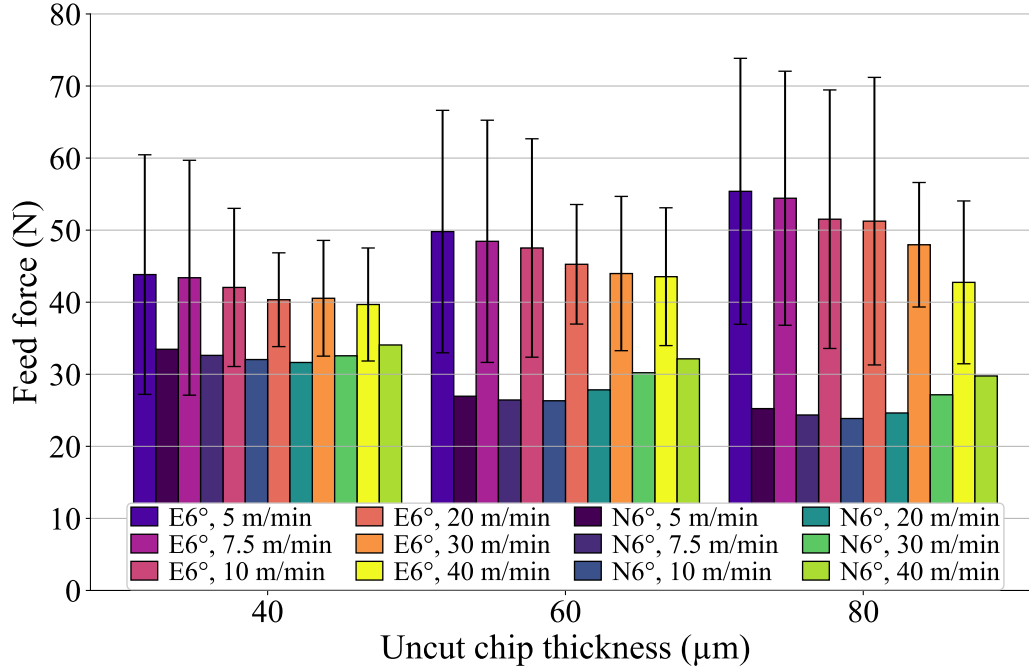


Figure 12: Comparison of experimental (E) and numerical (N) feed forces at the cutting edge inclination of 6° for the 3 uncut chip thicknesses (40, 60 and 80 μm) and the 6 cutting speeds (5, 7.5, 10, 20, 30 and 40 m/min)

337 Coupled with the differences in trends, this shows that F_f is less well modelled
338 (the average difference is 39 %) than F_c as usual in FE modelling of the cutting
339 process and even more so in 3D [12]. The influence of the uncut chip thickness
340 on the feed force should therefore be improved. The parameters of the material
341 constitutive model are known to have an impact on the forces (and on the chip
342 morphology) [26, 29]. The friction model should also be improved to strengthen
343 the results [12].

344 The passive force is non-zero for the inclination angle of 6° (Figure 13). Like
345 the cutting force, it increases with the uncut chip thickness and decreases with
346 the cutting speed. The comparison with experiments is broadly the same as for
347 F_c , except for a greater difference in the magnitude of F_p (the average difference
348 is 26 %, but it is small in absolute terms – less than 5 N). Most of the numerical
349 values do not fall within the experimental 95 % confidence interval. A lower mag-
350 nitude of the passive force from the simulation than from the experiments with
351 the correct trends when the cutting conditions change was also observed by Hardt

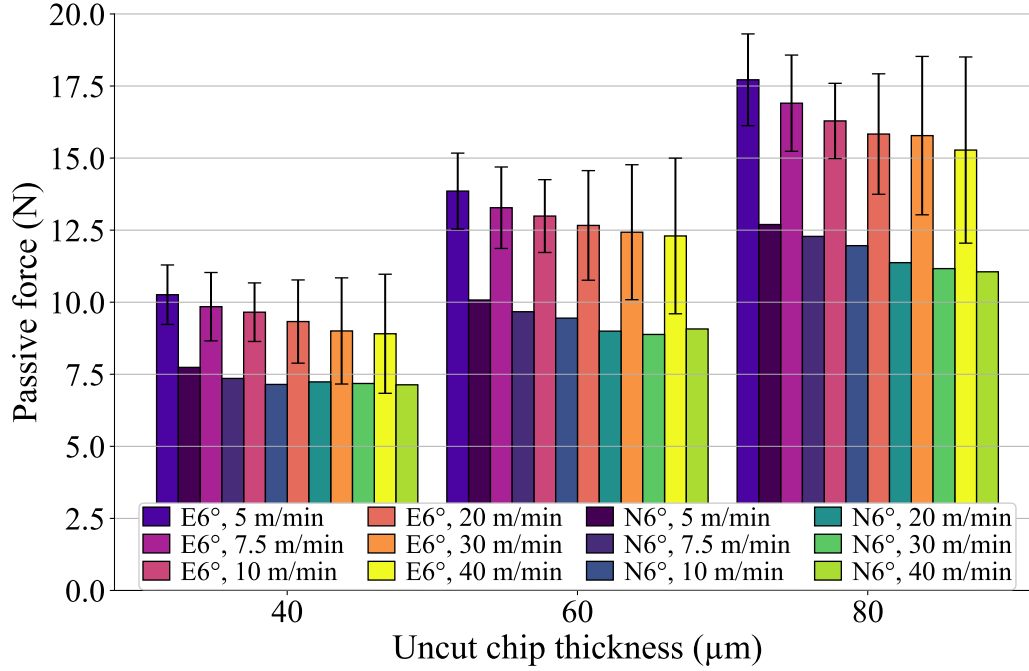


Figure 13: Comparison of experimental (E) and numerical (N) passive forces at the cutting edge inclination of 6° for the 3 uncut chip thicknesses (40, 60 and 80 μm) and the 6 cutting speeds (5, 7.5, 10, 20, 30 and 40 m/min)

and Bergs [12]. The differences were mainly attributed to differences in cutting edge radius, friction modelling and material constitutive model. In this work, the impact of the cutting edge radius can be neglected as it is the same in the model as in the experiments.

As far as the chip morphology is concerned, all chips are continuous. For both the simulation and the experiments, the chip thickness ratio, λ_h :

$$\lambda_h = \frac{h'}{h} \quad (13)$$

with h the uncut chip thickness and h' the chip thickness, is almost independent of the uncut chip thickness (Figures 14 and 15). It is slightly reduced from $\lambda_s = 0^\circ$ to $\lambda_s = 6^\circ$, which means that the chip thickness decreases with the inclination angle. This influence is underestimated by the model: the reduction of λ_h is smaller than in the experiments. The average difference between the experimental and numerical λ_h is 17 % over the whole range of cutting conditions. The chip thickness ratio

362 decreases with cutting speed due to the reduction in friction, which is correctly ac-
 363 counted for by the model. As with the feed force, the results should be improved
 364 by more complex friction models and a set of material parameters for which the
 365 identification includes forces and chip thickness: [26].

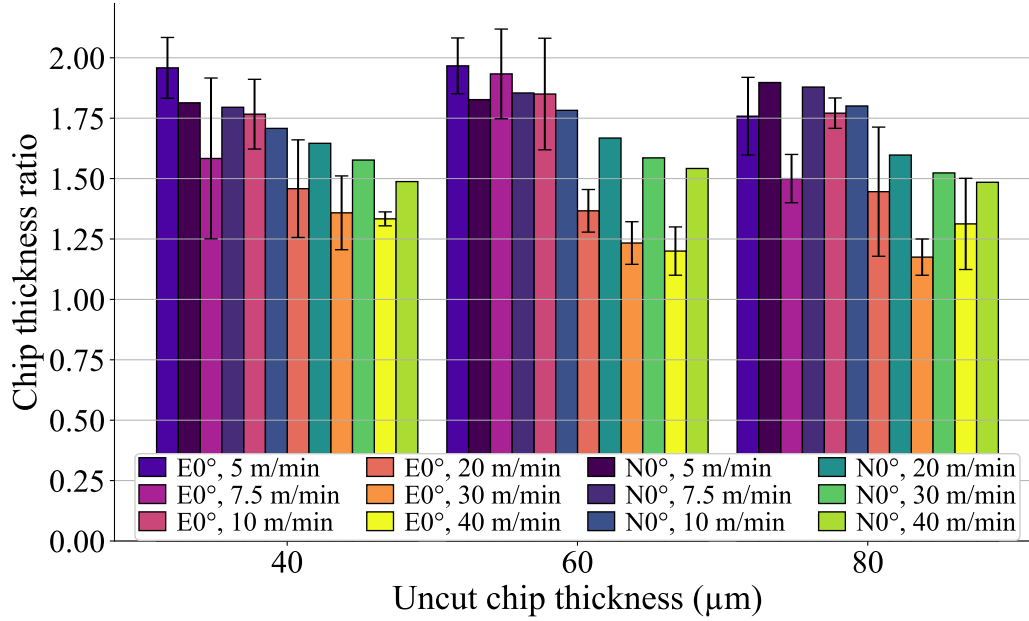


Figure 14: Comparison of experimental (E) and numerical (N) chip thickness ratios at the cutting edge inclination of 0° for the 3 uncut chip thicknesses (40, 60 and 80 μm) and the 6 cutting speeds (5, 7.5, 10, 20, 30 and 40 m/min)

366 The differences calculated according to the equation (12) are presented in Ta-
 367 ble 6 to provide a quantitative overview of the results. The cutting force is the best
 368 modelled quantity as observed in the literature. This result was to be expected as
 369 the parameter set of the constitutive model was selected mainly due to its good
 370 approximation of the cutting force [29]. As this selection was made with a 2D
 371 model, the results show the ability of the model to correctly handle the third (pas-
 372 sive) force. Based on the average differences, the performance of the model is very
 373 close for the cutting and feed forces for both cutting edge inclinations, although
 374 a small degradation (1 % and 2 %, respectively) is noted for 6°. This degradation
 375 is more important (7 %) for the chip thickness ratio and must be linked to the dif-
 376 ference in passive force. Indeed, the chip thickness and out-of-plane force models
 377 are deeply linked. Improving the friction at the tool-workpiece interface should

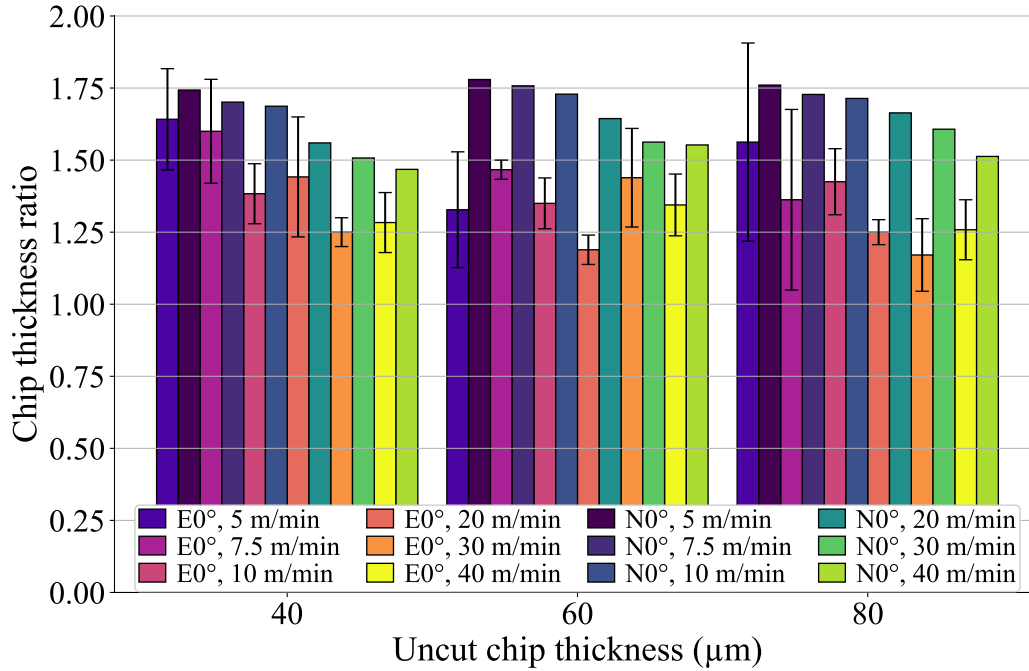


Figure 15: Comparison of experimental (E) and numerical (N) chip thickness ratios at the cutting edge inclination of 6° for the 3 uncut chip thicknesses (40, 60 and 80 μm) and the 6 cutting speeds (5, 7.5, 10, 20, 30 and 40 m/min)

be a key point. It should be noted that the chip thickness is very well modelled under certain cutting conditions with a minimum difference of 2 %. The difference is larger for the feed force than for the passive force, a trend opposite to that of Hardt and Bergs [12]. The average and range (min – max) of the differences are larger for the feed force. The smaller range of the passive force confirms a shift for all cutting conditions, similar to the results of Hardt and Bergs [12]. Again, the friction modelling should be the first aspect of the model to be improved in future developments.

5. Conclusions

An experimental and numerical study of the orthogonal and oblique free cutting of Ti6Al4V was carried out for a wide range of cutting conditions using an ANN-based material constitutive model. The following main conclusions are drawn:

Table 6: Synthetic quantitative overview of the results: differences between the experimental and the numerical results (average difference for each cutting edge inclination, and maximal, minimal and average differences for all the conditions) for the cutting force, ΔF_c , the feed force, ΔF_f , the passive force, ΔF_p , and the chip thickness ratio, $\Delta \lambda_h$

Difference	ΔF_c (%)	ΔF_f (%)	ΔF_p (%)	$\Delta \lambda_h$ (%)
Average $\lambda_s = 0^\circ$	3	38	–	14
Average $\lambda_s = 6^\circ$	4	40	26	21
Max. global	10	60	29	38
Min. global	1	10	19	2
Average global	4	39	26	17

- The experimental study was carried out with the same set-up in free orthogonal and free oblique cutting for the titanium alloy Ti6Al4V (the only change is the cutting edge inclination). This is a reference to evaluate the performance of the FE 3D model introducing an ANN-based constitutive model developed under the same conditions. An unpreviously seen wide range of cutting conditions, 36, is considered, including 2 cutting edge inclinations.
- A major novelty of this work is the accurate evaluation of the fundamental variables and their trends in 3D, without the need to adjust the numerical parameters and the model characteristics when the cutting conditions and the inclination angle are changed significantly. The mere fact of changing the inclination angle from free orthogonal cutting to oblique cutting while maintaining the quality of the results has no equivalent in the current literature, especially since no studies (experimental or numerical) on free oblique cutting are available.
- Taking into account the material's flow law by means of a neural network makes it possible to overcome the limitations of conventional flow laws and to reduce the approximations associated with the establishment of an analytical formulation of the flow law as conventionally adopted. The numerical model is then able to better reproduce the real behaviour of the material and to take into account thermomechanical transformations which are sources of non-linearities, difficult to take into account with an analytical flow law model. Current work, using a Gleeble thermomechanical simulator, on the

behaviour of a modified carbon alloy AISI P20 shows the advantages of this approach compared to models in the literature such as Johnson-Cook, Zerilli-Armstrong [16] or Hansel-Spittel [40], insofar as one is then able to better reproduce more complex material behaviours.

- The cutting force is the best modelled quantity with an average difference of 4 % with the experiments. Chip thickness ratio and passive force show a larger deviation from the experiments (17 % and 26 %, respectively), but their trends as the cutting conditions change are accurate. This is in line with the expected results provided by a predictive model. The deviation for feed force is higher (39 %), and opposite trends compared to the experimental reference are observed. The lack of influence of uncut chip thickness on friction in the model seems to be one of the aspects to be included as a priority in future work. The model is found to handle the occurrence of the third force, out of plane, well without significant degradation of the results.
- The predictive capabilities of the model make it suitable for the development of straight-edged tools, for example. This work also demonstrates the ability to model material behaviour with ANN and opens up possibilities in this promising direction.

References

- [1] P. J. Arrazola, T. Özel, D. Umbrello, M. Davies, I. S. Jawahir, Recent advances in modelling of metal machining processes, *CIRP Annals* 62 (2013) 695–718.
- [2] M. Agmell, V. Bushlya, S. V. A. Laakso, A. Ahadi, J.-E. Ståhl, Development of a simulation model to study tool loads in pcBN when machining AISI 316L, *Int J Adv Manuf Technol* 96 (2018) 2853–2865.
- [3] X. Xu, J. Outeiro, J. Zhang, B. Li, W. Zhao, Simulation of material side flow using a 3D coupled Eulerian-Lagrangian approach and a constitutive model considering the stress state, *Procedia CIRP* 102 (2021) 441–446.
- [4] M. Abouridouane, T. Bergs, D. Schraknepper, G. Wirtz, Friction behavior in metal cutting: Modeling and simulation, *Procedia CIRP* 102 (2021) 405–410.

- 445 [5] F. Ducobu, E. Rivière-Lorphèvre, E. Filippi, Experimental contribution to
446 the study of the Ti6Al4V chip formation in orthogonal cutting on a milling
447 machine, *Int J Mater Form* 8 (2015) 455–468.
- 448 [6] A. Sela, G. Ortiz-de-Zarate, D. Soler, G. Germain, P. Aristimuño, P. J. Arra-
449 zola, Measurement of plastic strain and plastic strain rate during orthogonal
450 cutting for Ti-6Al-4V, *International Journal of Mechanical Sciences* 198
451 (2021) 106397.
- 452 [7] M. Afrasiabi, J. Saelzer, S. Berger, I. Iovkov, H. Klippel, M. Röthlin,
453 A. Zabel, D. Biermann, K. Wegener, A Numerical-Experimental Study on
454 Orthogonal Cutting of AISI 1045 Steel and Ti6Al4V Alloy: SPH and FEM
455 Modeling with Newly Identified Friction Coefficients, *Metals* 11 (2021)
456 1683.
- 457 [8] F. Ducobu, E. Rivière-Lorphèvre, E. Filippi, Application of the Coupled
458 Eulerian-Lagrangian (CEL) method to the modeling of orthogonal cutting,
459 *Eur J Mech A Solids* 59 (2016) 58–66.
- 460 [9] F. Ducobu, E. Rivière-Lorphèvre, E. Filippi, Finite element modelling of 3D
461 orthogonal cutting experimental tests with the Coupled Eulerian-Lagrangian
462 (CEL) formulation, *Finite Elements in Analysis and Design* 134 (2017) 27–
463 40.
- 464 [10] D. Ambrosio, A. Tongne, V. Wagner, G. Dessein, O. Cahuc, A new damage
465 evolution criterion for the coupled Eulerian-Lagrangian approach: Applica-
466 tion to three-dimensional numerical simulation of segmented chip formation
467 mechanisms in orthogonal cutting, *Journal of Manufacturing Processes* 73
468 (2022) 149–163.
- 469 [11] A. Vovk, J. Sölter, B. Karpuschewski, Finite element simulations of the
470 material loads and residual stresses in milling utilizing the CEL method,
471 *Procedia CIRP* 87 (2020) 539–544.
- 472 [12] M. Hardt, T. Bergs, Three Dimensional Numerical Modeling of Face Turn-
473 ing Using the Coupled-Eulerian-Lagrangian Formulation, *Procedia CIRP*
474 102 (2021) 162–167.
- 475 [13] S. N. Melkote, W. Grzesik, J. Outeiro, J. Rech, V. Schulze, H. Attia, P.-J.
476 Arrazola, R. M’Saoubi, C. Saldana, Advances in material and friction data
477 for modelling of metal machining, *CIRP Annals* 66 (2017) 731–754.

- 478 [14] G. Johnson, W. Cook, A constitutive model and data for metals subjected
479 to large strains, high strain rates and high temperatures, in: Proc. 7th Inter-
480 national Symposium on Ballistics, volume 21, The Hague, The Netherlands,
481 pp. 541–547.
- 482 [15] M. Calamaz, D. Coupard, F. Girot, A new material model for 2D numer-
483 ical simulation of serrated chip formation when machining titanium alloy
484 Ti–6Al–4V, *International Journal of Machine Tools and Manufacture* 48
485 (2008) 275–288.
- 486 [16] A. M. Lennon, K. T. Ramesh, On the performance of modified Zerilli-
487 Armstrong constitutive model in simulating the metal-cutting process, *Jour-
488 nal of Manufacturing Processes* 28 (2017) 253–265.
- 489 [17] T. Özel, T. Altan, Determination of workpiece flow stress and friction at the
490 chip–tool contact for high-speed cutting, *Int J Mach Tools Manuf* 40 (2000)
491 133–152.
- 492 [18] A. Shrot, M. Bäker, Determination of Johnson–Cook parameters from ma-
493 chining simulations, *Comput Mater Sci* 52 (2012) 298–304.
- 494 [19] F. Klocke, D. Lung, S. Buchkremer, I. S. Jawahir, From Orthogonal Cutting
495 Experiments towards Easy-to-Implement and Accurate Flow Stress Data,
496 *Materials and Manufacturing Processes* 28 (2013) 1222–1227.
- 497 [20] P. Bosetti, C. Maximiliano Giorgio Bort, S. Bruschi, Identification of John-
498 son–Cook and Tresca’s Parameters for Numerical Modeling of AISI-304
499 Machining Processes, *J Manuf Sci Eng* 135 (2013).
- 500 [21] B. Denkena, T. Grove, M. A. Dittrich, D. Niederwestberg, M. Lahres, In-
501 verse Determination of Constitutive Equations and Cutting Force Modelling
502 for Complex Tools Using Oxley’s Predictive Machining Theory, *Procedia
503 CIRP* 31 (2015) 405–410.
- 504 [22] T. Bergs, M. Hardt, D. Schraknepper, Determination of Johnson-Cook ma-
505 terial model parameters for AISI 1045 from orthogonal cutting tests using
506 the Downhill-Simplex algorithm, *Procedia Manuf* 48 (2020) 541–552.
- 507 [23] M. Hardt, D. Schraknepper, T. Bergs, Investigations on the Application of
508 the Downhill-Simplex-Algorithm to the Inverse Determination of Material

- 509 Model Parameters for FE-Machining Simulations, *Simulation Modelling*
510 *Practice and Theory* 107 (2021) 102214.
- 511 [24] B. Stampfer, G. González, E. Segebade, M. Gerstenmeyer, V. Schulze, Ma-
512 terial parameter optimization for orthogonal cutting simulations of AISI4140
513 at various tempering conditions, *Procedia CIRP* 102 (2021) 198–203.
- 514 [25] M. Hardt, D. Jayaramaiah, T. Bergs, On the Application of the Particle
515 Swarm Optimization to the Inverse Determination of Material Model Pa-
516 rameters for Cutting Simulations, *Modelling 2* (2021) 129–148.
- 517 [26] N. Kugalur Palanisamy, E. Rivière Lorphèvre, M. Gobert, G. Briffoteaux,
518 D. Tuytens, P.-J. Arrazola, F. Ducobu, Identification of the Parameter Val-
519 ues of the Constitutive and Friction Models in Machining Using EGO Algo-
520 rithm: Application to Ti6Al4V, *Metals* 12 (2022) 976.
- 521 [27] O. Pantalé, P. Tize Mha, A. Tongne, Efficient implementation of non-linear
522 flow law using neural network into the Abaqus Explicit FEM code, *Finite*
523 *Elements in Analysis and Design* 198 (2022) 103647.
- 524 [28] S. Seo, O. Min, H. Yang, Constitutive equation for Ti–6Al–4V at high tem-
525 peratures measured using the SHPB technique, *Int J Impact Eng* 31 (2005)
526 735–754.
- 527 [29] F. Ducobu, E. Rivière-Lorphèvre, E. Filippi, On the importance of the choice
528 of the parameters of the Johnson-Cook constitutive model and their influence
529 on the results of a Ti6Al4V orthogonal cutting model, *Int J Mech Sci* 122
530 (2017) 143–155.
- 531 [30] GRANTA EduPack 2020, Granta Design Limited, 2020.
- 532 [31] N. Milošević, I. Aleksic, Thermophysical properties of solid phase Ti-6Al-
533 4V alloy over a wide temperature range (2012).
- 534 [32] J. Rech, P. J. Arrazola, C. Claudin, C. Courbon, F. Pusavec, J. Kopac, Char-
535 acterisation of friction and heat partition coefficients at the tool-work mate-
536 rial interface in cutting, *CIRP Annals* 62 (2013) 79–82.
- 537 [33] O. Pantalé, Coefficients of an ANN constitutive flow law of a Ti6-Al-4V
538 material for dynamic applications, *Zenodo* (2022).

- [34] L. Wang, H. Long, Investigation of material deformation in multi-pass conventional metal spinning, *Materials & Design* 32 (2011) 2891–2899.
- [35] F. Ducobu, E. Rivière-Lorphèvre, E. Filippi, On the introduction of adaptive mass scaling in a finite element model of Ti6Al4V orthogonal cutting, *Simulation Modelling Practice and Theory* 53 (2015) 1–14.
- [36] M. Sima, T. Özel, Modified material constitutive models for serrated chip formation simulations and experimental validation in machining of titanium alloy Ti–6Al–4V, *International Journal of Machine Tools and Manufacture* 50 (2010) 943–960.
- [37] F. Ducobu, E. Rivière-Lorphèvre, E. Filippi, Material constitutive model and chip separation criterion influence on the modeling of Ti6Al4V machining with experimental validation in strictly orthogonal cutting condition, *International Journal of Mechanical Sciences* 107 (2016) 136–149.
- [38] Y. Karpas, Temperature dependent flow softening of titanium alloy Ti6Al4V: An investigation using finite element simulation of machining, *Journal of Materials Processing Technology* 211 (2011) 737–749.
- [39] Y. C. Zhang, T. Mabrouki, D. Nelias, Y. D. Gong, Chip formation in orthogonal cutting considering interface limiting shear stress and damage evolution based on fracture energy approach, *Finite Elements in Analysis and Design* 47 (2011) 850–863.
- [40] K. Chadha, D. Shahriari, M. Jahazi, An approach to develop hansel–spittel constitutive equation during ingot breakdown operation of low alloy steels, in: *Frontiers in materials processing, applications, research and technology*, Springer, 2018, pp. 239–246.

Appendix A. Coefficients of the ANN 3-9-7-1-sig

In this appendix, we present the values obtained after the training phase of an ANN containing 9 neurons in the first hidden layer and 7 neurons in the second hidden layer. Conforming to [27], this one is referred ANN-3-9-7-1-sig. The training of the neural network was performed using a dataset containing 3430 data points defined by:

- 70 equidistant values for $\varepsilon^p \in [0, 3]$, so that $[\varepsilon^p]_{min} = 0$ and $[\varepsilon^p]_{max} = 3$.

- 7 plastic strain rates $\dot{\epsilon}^p \in [1/\text{s}, 10/\text{s}, 50/\text{s}, 500/\text{s}, 5000/\text{s}, 50\,000/\text{s}, 500\,000/\text{s}]$, so that $[\ln(\dot{\epsilon}^p)]_{\min} = 0$ and $[\ln(\dot{\epsilon}^p)]_{\max} = 13.12236$.
- 7 temperatures $T \in [293\text{ K}, 400\text{ K}, 500\text{ K}, 700\text{ K}, 900\text{ K}, 1200\text{ K}, 1500\text{ K}]$, so that $[T]_{\min} = 293\text{ K}$ and $[T]_{\max} = 1500\text{ K}$.

Stresses in the training dataset ranges from $[\sigma^y]_{\min} = 171.4\text{ MPa}$ to $[\sigma^y]_{\max} = 2606.1\text{ MPa}$. The results of the training process are given here after for the ANN quantities \mathbf{W}_1 , \mathbf{W}_2 , \vec{w} , \vec{b}_1 , \vec{b}_2 and b . The weight matrix for the first hidden layer \mathbf{W}_1 is a 9×3 matrix:

$$\mathbf{W}_1 = \begin{bmatrix} -0.87229 & -0.47675 & -1.50771 \\ -0.95762 & -0.25619 & 1.65222 \\ -10.61660 & 0.22003 & -0.11539 \\ 3.67883 & 0.37146 & -1.51069 \\ -63.39468 & 0.15466 & -0.95431 \\ 0.54807 & 0.25959 & -5.44355 \\ -1.33883 & 0.36089 & -1.66735 \\ -0.68125 & 1.02121 & 0.34242 \\ 0.08740 & 0.18764 & -41.32542 \end{bmatrix}$$

The weight matrix for the second hidden layer \mathbf{W}_2 is a 7×9 matrix:

$$\mathbf{W}_2^T = \begin{bmatrix} 1.66285 & -0.59645 & -3.17333 & 0.20706 & 1.18760 & 2.01250 & -0.82147 \\ -0.26237 & -2.50330 & -1.45941 & -1.59833 & 4.05169 & -1.21146 & 1.05610 \\ -0.12958 & 0.67119 & -5.85989 & -2.55061 & 4.85245 & 4.31876 & 3.24070 \\ -2.12890 & 0.68296 & 0.71183 & 0.81706 & -0.09405 & 0.34919 & -1.41223 \\ 2.33631 & -0.08089 & 14.65789 & 0.12531 & 23.66363 & 2.55872 & 2.15338 \\ 0.11567 & 1.77629 & -1.80448 & 0.77825 & -1.58254 & 1.90442 & 1.23152 \\ 1.49265 & 0.41821 & -3.53803 & -0.48705 & -0.23671 & 0.75887 & -0.37441 \\ 0.95990 & 0.69041 & 0.43870 & 0.28393 & -1.40101 & -0.64569 & -0.38964 \\ 5.89937 & -0.13015 & 2.99264 & 1.78534 & -3.90189 & 1.17494 & -3.78854 \end{bmatrix}$$

The weight vector for the output layer \vec{w} is a 7 components vector:

$$\vec{w} = \begin{bmatrix} 0.34701 \\ 1.42079 \\ -0.96564 \\ 0.62467 \\ -0.56322 \\ 0.40960 \\ -0.42810 \end{bmatrix}$$

The biases of the first hidden layer \vec{b}_1 is a 9 components vector:

$$\vec{b}_1 = \begin{bmatrix} 2.57141 \\ 0.22673 \\ -1.16985 \\ -0.11246 \\ -0.82210 \\ -2.13264 \\ 0.78794 \\ 1.20434 \\ -3.48681 \end{bmatrix}$$

The biases of the second hidden layer \vec{b}_2 is a 7 components vector:

$$\vec{b}_2 = \begin{bmatrix} -0.36566 \\ -1.14445 \\ -0.79065 \\ -0.50670 \\ 1.30136 \\ 0.04521 \\ -0.29995 \end{bmatrix}$$

The bias of the output layer b is a scalar:

$$b = 0.04213$$

580 The corresponding coefficients for the other networks identified during this
581 work (ANN-3-11-7-1-sig, ANN-3-13-7-1-sig, ANN-3-15-7-1-sig and ANN-3-17-
582 7-1-sig) can be found in [33].